JOURNAL OF PROPULSION AND POWER
Vol. 13, No. 4, July–August 1997

Uncertainty Assessment of Performance Evaluation Methods for Solar Thermal Absorber/Thruster Testing

Pete Markopoulos,* Hugh W. Coleman,† and Clark W. Hawk‡
University of Alabama in Huntsville, Huntsville, Alabama 35899

Proposed ground testing of solar thermal upper stage propulsion systems will verify the technology readiness level and provide a higher degree of confidence for pursuing a flight experiment. This study applies experimental uncertainty analysis techniques to investigate various performance evaluation methods that could be used to interpret results of solar thermal absorber/thruster ground testing. A general uncertainty analysis is applied to engine specific impulse determination methods for an open-ended cavity, heat exchanger type, solar thermal engine. Six performance relationships consisting of both thrust- and nonthrust-based evaluation methods are utilized and two nominal operating cases are assessed. Based on the uncertainty estimates made for individual variables in the data reduction equations, overall specific impulse uncertainties for the nonthrust-based methods range from about 6 to 10%, depending on the method and testing situation. Thrust-based evaluation methods yield specific impulse uncertainties on the order of 1.5% if thrust and propellant mass flow rate can be measured with uncertainties of 1% or less.

Nomenclature

A_e = nozzle exit area
A_1 = solar absorber cavity interior area
A_2 = solar absorber cavity opening area
C, CR = concentration ratio
c_p = specific heat at constant pressure, Btu/lb mol °R
c_v = specific heat at constant volume, Btu/lb mol °R
D_e = nozzle exit diameter, in.
e_1 = emissivity of the inner cavity
e_2 = emissivity of the cavity opening
F = thrust, lbf
F_{ij} = view factor surface i to j
G_s = solar constant
g_c = dimensional conversion constant, lbm-ft/lbf-s^2
g_0 = gravitational acceleration at sea level, 32.174 ft/s^2
I_{sp} = specific impulse, s
k = thermal conductivity of fluid, mean, Btu/h-ft-°R
L = length of solar thermal cavity absorber, in.
L_t = length of coolant tube path, ft
M = molar mass of exit fluid
$\dot{m}$ = mass flow rate, lbm/s
P_c = chamber pressure, psia
P_e = nozzle exit pressure, psia
P_3 = ambient pressure, psia
R = radius of solar thermal cavity absorber, in.
R_c = universal gas constant
T_e = temperature of exit fluid at nozzle exit, °R
$T_{H_2 f}$, Tc = chamber temperature, °R
$T_{H_2 i}$ = inlet temperature of hydrogen fluid, °R
T_1 = average interior solar absorber cavity temperature
U_r = uncertainty in a result
α = absorptivity of inner cavity
γ = ratio of specific heats, c_p/c_v
ε_1 = emissivity of the inner cavity
ε_2 = emissivity of the cavity opening
θ = nozzle divergence half-angle, deg
λ_N = nozzle divergence factor
σ = Stefan–Boltzmann constant

Presented as Paper 96-3012 at the AIAA/ASME/SAE/ASEE 32nd Joint Propulsion Conference, Lake Buena Vista, FL, July 1–3, 1996; received Aug. 20, 1996; revision received Feb. 15, 1997; accepted for publication Feb. 27, 1997.

*Graduate Research Assistant, Propulsion Research Center, Department of Mechanical and Aerospace Engineering; currently at Lockheed Martin Astronautics. Student Member AIAA.

†Eminent Scholar in Propulsion, Professor, Propulsion Research Center, Department of Mechanical and Aerospace Engineering. Associate Fellow AIAA.

‡Professor, Department of Mechanical and Aerospace Engineering, Director, Propulsion Research Center. Associate Fellow AIAA.

Introduction

THE solar thermal upper stage (STUS) is a high-performance upper stage capable of transferring payloads from low Earth orbit (LEO) to geosynchronous orbit (GEO) in 15–30 days. An example of a solar-thermal-propulsion-based orbital vehicle is represented in Fig. 1. The STUS can nearly double the GEO payload of expendable launch vehicles compared to traditional chemical transfer stages. It can also provide the means to accomplish interorbital, lunar, or interplanetary transfer missions. Design and development of a solar thermal propulsion orbit transfer vehicle has been pursued by NASA Marshall Space Flight Center.[1] The system utilizes hydrogen with an engine-calculated specific impulse of 860 s to deliver payload to a specified orbit for a given launch vehicle. It was designed to serve as an upper stage for a Lockheed Martin Missiles & Space Company LLV3 launch vehicle.

Solar thermal propulsion operates on a simple and basic propulsion concept. The concept makes use of an available energy source, the sun, to convert radiant solar energy to thermal energy to kinetic energy in the form of a propulsive thrust.

By using compressible flow relationships,[2] it can be shown that the specific impulse is proportional to the square root of the chamber temperature divided by the molecular mass of the engine exhaust products $(T_c/M)^{1/2}$. Increasing chamber temperatures T_c and/or decreasing molecular weight M of exhaust products increases the specific impulse. Use of hydrogen as the working fluid for a solar thermal propulsion engine provides the potential for a very high specific impulse and can be used to regeneratively cool the absorber and thruster compo-

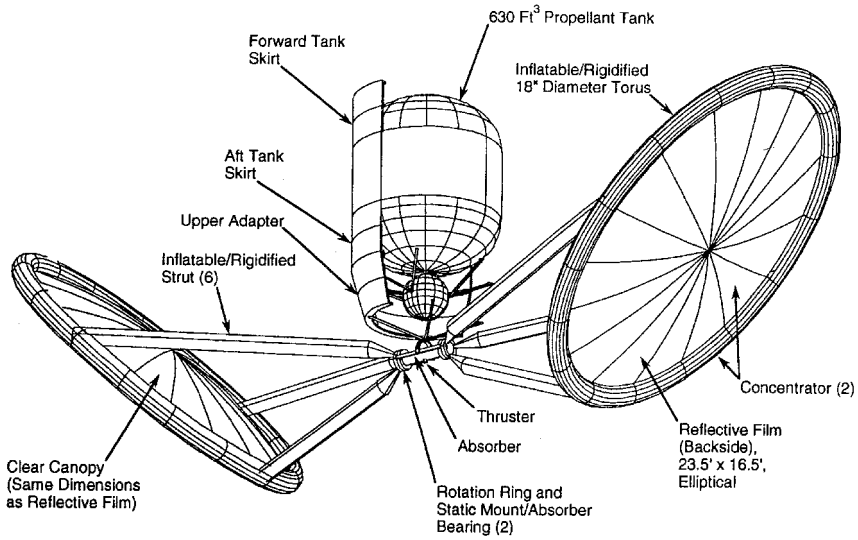

Fig. 1 STUS.

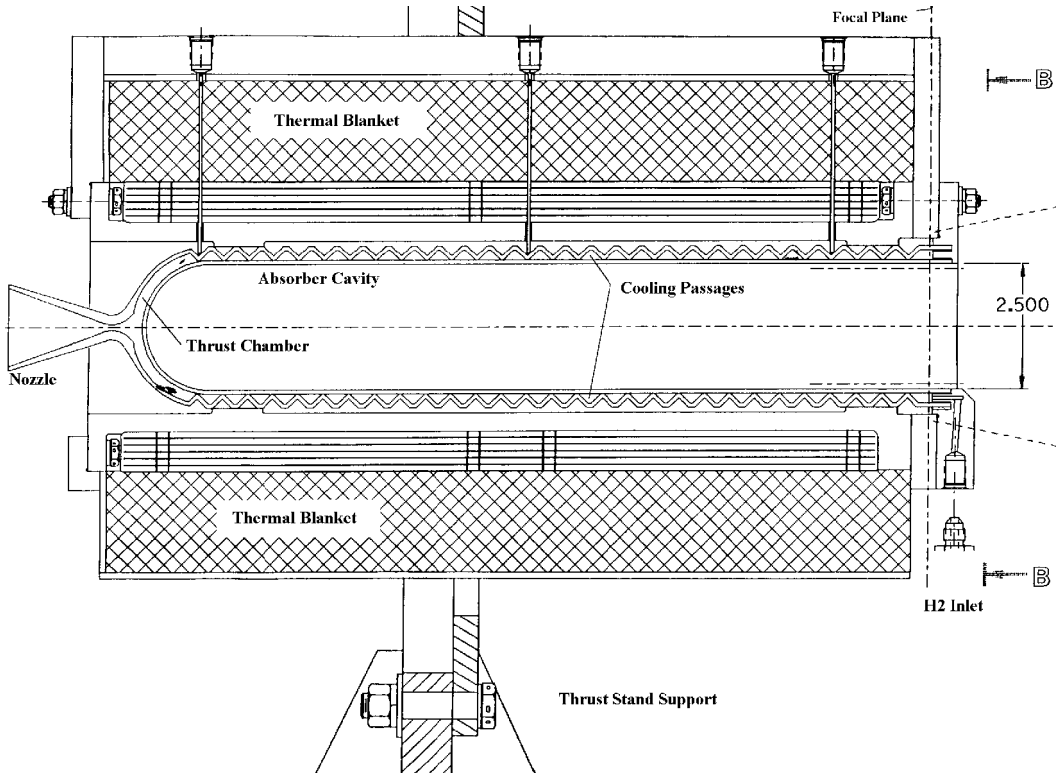

Fig. 2 Solar thermal engine.

nents. Because of the low molecular weight of H_2, the exhaust velocities and specific impulses are much greater than those for the chemical combustion of fuel.

Recent testing and analyses of solar thermal technology have been performed by various organizations. Testing of a coiled rhenium-tube cavity heat exchanger and thruster has been performed at the U.S. Air Force Phillips Laboratories, Edwards, California.[3] This solar thermal propulsion unit was designed to be capable of accepting 20 kW of thermal power at a design temperature of 5000°R (2778 K) and to yield a specific impulse of 810 s. The test unit was successfully operated for a total duration of 65 h, achieving a maximum gas temperature of 3260°R (1810 K), which translates to 650 s of calculated I_{sp}.

The primary objective of this current research program was to apply a general uncertainty analysis to performance–evaluation methods that could be utilized in solar thermal absorber/thruster testing. Nominal values used in the general uncertainty analysis of the performance evaluation methods are obtained from previous predictions and engine model design considerations. Evaluating testing techniques and data reduction methodologies via a general uncertainty analysis provides insight to distinguish variable measurements most influencing the overall result uncertainty. Once the critical measurements are identified, means to lower these uncertainties can be explored to yield lower result uncertainties.

Solar Thermal Engine

The engine used in this study utilizes the windowless solar thermal absorber concept. Figure 2 shows a solar thermal propulsion engine design using an open-ended cavity absorber[4]

that is a long cylinder open on one end with the opposite end formed with a hemispherical end cap. The long cylindrical construction of the cavity allows most of the radiation that is reflected or emitted to impinge upon other sections of the internal cavity. Light rays entering the cavity are reflected to the rear wall of the absorber unit where energy is absorbed by the working fluid in the heat exchanger arrangement.

This engine is currently being fabricated by NASA in conjunction with the STUS technology demonstrator program consortium. The absorber consists of two interconnected shells and is constructed from 100% tungsten that is vapor deposited onto graphite mandrels to meet design specifications.

The inner shell of the absorber is fabricated by depositing the material onto a cylindrical mandrel with a hemispherical end cap (16.7 in. long × 2.51 in. diam × 0.08 in. thick). The outer shell of the absorber is also fabricated in the same manner, although the material is deposited onto a graphite mandrel that has grooves oriented in a helical fashion resembling screw threads. Once the shell is made, the graphite core is screwed out of the assembly. The inner shell is then inserted into the outer shell providing the capability to pass fluid between the grooves of the interface traversing the length of the absorber through a helical path to the hemispherical end between the solar absorber shells. The shells are attached through an interference fit between the teeth of the outer shell and the contact surface of the inner shell and brazed together at the cavity opening.

A solar concentrator is utilized to collect and focus concentrated solar energy into the cavity. Radiation exchange takes place, whereby thermal energy is transferred from the cavity surface to the flowing fluid. Two inlets at the opening of the cavity allow fluid to enter the cooling passages and two outlets at the end of the cavity allow the heated fluid to enter the chamber. At this point the fluid is then expanded out a conical nozzle with an expansion ratio of 100:1 and a throat diameter of approximately 0.13 in. (Nozzle length is 2.5 in. with a divergence half-angle of 20 deg.)

This assembly is surrounded by layers of thin tungsten sheets that serve as radiation shields. Covering the assembly is a thick blanket of insulative material that reduces heat transfer to the surroundings. The entire unit is supported by an interface flange at its c.m. attached to a thrust stand within an altitude chamber where the pressure is evacuated.

Performance Evaluation Methods

Six methods were used in this study for determining the specific impulse performance of a solar thermal cavity absorber propulsion unit. The methods include both a thrust-based and variety of nonthrust-based evaluation procedures. The nonthrust-based methods (methods 2–6) are derived from one-dimensional representations involving assumptions for ideal flow and assumptions made in the evaluation of the absorber cavity and chamber temperatures.[5,6]

A schematic of the solar absorber/thruster is shown in Fig. 3. The model represents a heat-exchanger-type open-ended-cavity absorber solar thermal engine.

Thrust-Based Evaluation Method

Method 1

Method 1 involves a direct measurement of engine thrust and mass flow rates. The specific impulse is defined as the thrust divided by propellant weight flow rate[2] and is given by

$$I_{sp1} = (F/\dot{m})(g_c/g_0) \tag{1}$$

where g_c is 32.174 (lbm-ft)/(lbf-s^2) in the English system and 1.0 (dimensionless) in the SI system. In all of the following equations, g_c is omitted.

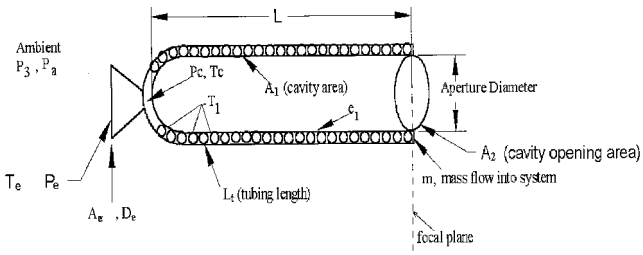

Fig. 3 Simplified solar engine model.

Nonthrust-Based Evaluation Methods

Method 2

Method 2 involves the use of ideal rocket relationships.[2] Method 2 also evaluates the specific impulse of an engine in terms of a chamber temperature (T_c or $T_{H_2 f}$), P_c, P_e, P_3 and mass flow rate:

$$I_{sp2} = \sqrt{\frac{2R_c}{g_0^2}\left(\frac{\gamma}{\gamma-1}\right)\left(\frac{T_{H_2 f}}{M}\right)\left[1-\left(\frac{P_e}{P_c}\right)^{(\gamma-1)/\gamma}\right]} + \frac{(P_e - P_3)\pi D_{\text{exit}}^2}{4\dot{m}g_0} \tag{2}$$

The relationship is based on the assumption that there is no change in the composition of the exhaust gas as it progresses through the nozzle.

Method 3

Method 3 couples heat transfer theory and the relationship of method 2 to yield an estimate of specific impulse for a solar thermal engine. Method 2 utilizes the measurement of a chamber temperature to estimate a specific impulse, whereas, method 3 uses an indirect relationship as a substitute for a chamber temperature.

By simplifying the cavity design to one resembling a cylinder, view factors relating radiation exchange ratios between cavity internal surfaces, assumed to be at a single temperature T_1, and the absorber opening aperture can be determined. The energy balance yields equations relating solar absorber cavity efficiency and absorber cavity temperature. In addition, the working fluid was analyzed through the use of energy relationships to yield an estimate of fluid temperature along the length of the absorber cavity as a function of cavity internal surface area. The resulting expression for the expected fluid temperature in the chamber $T_{H_2 f}$ as a function of ε_1, ε_2, α_{cavity}, L/D, CR, L_t, and mass flow rate is as follows:

$$T_c = T_{H_2 f} = \left\{ \frac{T_{H_2 i} + \dfrac{4.36k\sqrt[4]{\dfrac{CG_s A_2}{\varepsilon_1 A_1 \sigma[1.0 + (\alpha/\varepsilon_1)\varepsilon_2 F_{12}]}}(\pi L_t)}{\dot{m}c_p}}{1 + (4.36k\pi L_t/\dot{m}c_p)} \right\} \tag{3}$$

where A_1 and A_2 are functions of absorber cavity length and diameter, and the view factor F_{12} is related by absorber cavity length to aperture radius ratio:

$$F_{12} = 1 + \left(\frac{R}{2L} - 1\right)\left\{\frac{1}{2}\left[\frac{L}{R}\sqrt{4 + \left(\frac{L}{R}\right)^2} - \left(\frac{L}{R}\right)^2\right]\right\} \tag{4}$$

Substituting into method 2 for the chamber temperature, T_c yields the following:

$$I_{sp3} = \sqrt{\frac{2R_c}{g_0^2}\left(\frac{\gamma}{\gamma - 1}\right)\left(\frac{\left\{T_{H_2 i} + \dfrac{4.36k\sqrt[4]{\dfrac{G_s C A_2}{\varepsilon_1 A_1 \sigma[1.0 + (\alpha/e_1)e_2 F_{12}]}}(\pi L_t)}{\dot{m}c_p}\right\}}{M[1 + (4.36k\pi L_t/\dot{m}c_p)]}\right)\left[1 - \left(\frac{P_e}{P_c}\right)^{(\gamma-1)/\gamma}\right]} + \frac{(P_e - P_3)\pi D_{exit}^2}{4\dot{m}g_0} \tag{5}$$

Method 4

The one-dimensional model equations assume that the exhaust gases exiting at the nozzle exit plane are axially directed. In reality, depending upon the nozzle geometric curvature, the exiting gases are directed at an angle to the nozzle centerline. This results in a loss of propulsive efficiency because of nozzle divergence effects. To compensate for the nonaxial behavior of the exhaust gas velocity profile, a theoretical correction factor can be applied to the momentum term of the thrust equation. Method 4 considers effects of nozzle divergence angle effects on performance. The λ_N is defined by

$$\lambda_N = \tfrac{1}{2}[1 + \cos(\theta)] \tag{6}$$

Modifying Method 2 specific impulse expression to account for this effect yields the following:

$$I_{sp4} = \left\{\frac{1}{2}[1 + \cos(\theta)]\right\} \times \sqrt{\frac{2R_c}{g_0^2}\left(\frac{\gamma}{\gamma - 1}\right)\left(\frac{T_c}{M}\right)\left[1 - \left(\frac{P_e}{P_c}\right)^{(\gamma-1)/\gamma}\right]} + \frac{(P_e - P_a)\pi D_{exit}^2}{4\dot{m}g_0} \tag{7}$$

Method 5

Whereas methods 2–4 are based upon a frozen equilibrium assumption, method 5 evaluates specific impulse assuming chemical equilibrium is maintained during the nozzle expansion process. In this case, reactions because of high-temperature dissociation and recombination of the single fluid are considered. The specific impulse is based on the exit velocity assuming a negligible nozzle gas flow inlet velocity. The specific impulse can be related in terms of chamber temperature, nozzle exit temperature and pressure, and ambient conditions:

$$I_{sp5} = \sqrt{\frac{2c_{p,\text{eff}}}{g_0^2}(T_c - T_{exit})\frac{1}{M}} + \frac{(P_e - P_3)\pi D_{exit}^2}{4\dot{m}g_0} \tag{8}$$

Typically, iterative calculations are performed in determining the level of dissociation at several points in the nozzle to obtain temperatures of the exhaust gas. The method that is used assumes that both a chamber and exit temperature can be measured to assess the performance.

Method 6

Method 6 is a combination of methods 5 and 3. The method involves the use of Eq. (3) as a substitute for a chamber temperature measurement in Eq. (8), and is represented by the following:

$$I_{sp6} = \sqrt{\frac{2c_{p,\text{eff}}}{g_0^2}\left\{\frac{T_{H_2 i} + \dfrac{4.36k\sqrt[4]{\dfrac{CG_s A_2}{\varepsilon_1 A_1 \sigma[1.0 + (\alpha/\varepsilon_1)\varepsilon_2 F_{12}]}}\pi L_t}{\dot{m}c_p}}{1 + (4.36k\pi L_t/\dot{m}c_p)} - T_{exit}\right\}\frac{1}{M}} + \frac{(P_e - P_3)\pi D_{exit}^2}{4\dot{m}g_0} \tag{9}$$

These methods do not consider performance losses caused by boundary layer effects that exist in small-throated solar thermal nozzles.[7] Previous computational fluid dynamics analyses have indicated that the boundary layers in these small nozzles can grow to a major fraction of the nozzle radius that can contribute to performance losses. Boundary-layer growth and size could be a large contributor to the result uncertainty, although this is not considered in this analysis. The losses are attributed to viscous drag on the nozzle walls and potential flow blockage by the boundary layer.

Uncertainty Analysis Procedure

In nearly all experiments, the measured values of different variables are combined into a data reduction equation (DRE) to form some desired result. Equations (1), (2), (5), (7–9) are examples of such DREs. A general representation of a data reduction equation is the following:

$$r = r(X_1, X_2, X_3, \ldots, X_j) \tag{10}$$

where r represents the experimental result determined from j measured variables (X_i). Each of the measured variables contains errors. These errors in the measured values then propagate through the DRE, thereby generating errors in r.

The overall U_r can be represented as

$$\frac{U_r}{r} = \left[\sum_{i=1}^{j}\left(\frac{X_i}{r}\frac{\partial r}{\partial X_i}\right)^2\left(\frac{U_{X_i}}{X_i}\right)^2\right]^{1/2} \tag{11}$$

or, equivalently, as

$$U_r = \left[\sum_{i=1}^{j}\left(\frac{\partial r}{\partial X_i}U_{X_i}\right)^2\right]^{1/2} \tag{12}$$

where U_{x_i} is the uncertainty in the variable X_i. The interval ($r \pm U_r$) contains the true (but unknown) value of r about 95% of the time.

A general uncertainty analysis was performed for this study. Therefore, the uncertainties of the variables were not considered separately in terms of bias and precision.[8] An estimate was made of the overall uncertainty of each variable. The uncertainty values were then propagated through the data reduction relationships previously designated as methods 1–6.

For cases in which the data reduction expression is very complex and the task of evaluating the partial derivatives is difficult, a finite difference approach can be employed, where

$$\left.\frac{\partial r}{\partial x_1}\right|_{x_2,\ldots x_{J_{\text{const}}}} \approx \frac{\Delta r}{\Delta x_1} = \frac{r_{x_1+\Delta x_1, x_2 \ldots x_J} - r_{x_1, x_2 \ldots x_J}}{\Delta x_1} \tag{13}$$

The finite difference approximation becomes

$$U_r^2 \cong \left(\frac{\Delta r}{\Delta x_1} U_{x_1}\right)^2 + \left(\frac{\Delta r}{\Delta x_2} U_{x_2}\right)^2 + \cdots + \left(\frac{\Delta r}{\Delta x_J} U_{x_J}\right)^2 \quad (14)$$

Such an approach was used in this study.

The sensitivity of the uncertainty of the result to the uncertainty of various measured quantities is presented in two ways: 1) the uncertainty magnification factor (UMF) (Ref. 9) and 2) the uncertainty percentage contribution (UPC) (Ref. 10). The UMF is defined as

$$\text{UMF} = \frac{X_i \partial r}{r \partial X_i} \quad (15)$$

The UMF determines the influence of the uncertainty in X_i as it propagates through the data reduction equation into the result if the uncertainties of all other variables are zero. The significance of the UMF can be seen by referring to Eq. (11). UMF values less than unity indicate diminishing effects on result uncertainty. The variable uncertainty diminishes as it propagates through the data reduction equation. UMF values greater than unity indicate the variable uncertainty increases as it propagates through the data reduction equation. This type of analysis is useful for a general case during the planning phase of an experiment. In this study all UMF values are presented as positive numbers. The sign does not affect the overall uncertainty since all terms are squared in the uncertainty Eq. (11).

UPC is defined as

$$\text{UPC} = \frac{\left(\frac{\partial r}{\partial X_i} U_{X_i}\right)^2}{\sum_{i=1}^{j} \left(\frac{\partial r}{\partial X_i} U_{X_i}\right)^2} \times 100 \quad (16)$$

By recognizing that the denominator is the total result uncertainty, Eq. (16) can be rewritten as

$$\text{UPC} = \frac{\left(\frac{\partial r}{\partial X_i} U_{X_i}\right)^2}{U_r^2} \times 100 \quad (17)$$

The UPC describes the influence of the product of the sensitivity coefficient and uncertainty for a variable as a percentage of the result uncertainty squared for each squared term. The significance of the UPC can be seen by referring to Eq. (12). This approach shows the sensitivity of the squared uncertainty of the result to the squared uncertainty effect of each of the variables for a particular situation where values for the variables are known and the uncertainties for each variable have been estimated. This type of analysis is useful during the later planning and early design phases of an experiment.

The uncertainty analysis techniques were applied to the performance evaluation methods to determine the result uncertainty corresponding to the particular method.

Operating Conditions and Uncertainty Estimates

Nominal values used in the performance analysis studies and in the general uncertainty analysis of performance evaluation methods were obtained from previous predictions.[11] Two cases were analyzed. The first case (case A) is based on a specific concentrator with an area of 374 ft^2 focusing onto the solar thermal absorber depicted in Fig. 2 with an equivalent concentration ratio of approximately 11,000:1. At this concentration ratio, the thermal input to the absorber cavity is approximately 47 kW, assuming the concentrator focal spot size is of the same diameter as the cavity opening aperture. The second case (case B) was based on a maximum solar flux intensity of 7161 W/in.^{2} into the same solar thermal absorber cavity. The solar intensity rating is derived from a 20 × 25 ft elliptical concentrator available at the Phillips Solar Laboratory Facility at the U.S. Edwards Air Force Base.[3] This solar testing facility is equipped with a rigid precision concentrator capable of providing approximately 25 kW of thermal energy onto an 8-in. elliptical focal plane. This will represent approximately 15.4 kW into the absorber cavity with a peak concentration ratio of 8000 onto an 8-in. focal plane. The resulting geometric concentration ratio is approximately 4000:1. Table 1 summarizes the nominal values of the variables for cases A and B.

Table 1 Nominal values of variables in cases A and B

Variable	Nominal value, case A	Nominal value, case B	Uncertainty estimate, %
R	1.25	1.25	1
L	17	17	1
e_1, ε_1	0.27	0.27	50
e_2, ε_2	1	1	1
CR	11000	4000	15
L_t	19.7	19.7	1
k	0.306	0.306	1
$T_{H_2 i}$	600	600	10
a, α	0.6	0.6	50
P_e	0.15	0.15	10
P_c	15	15	10
c_v	5.44	5.25	1
c_{p1}	7.43	7.24	1
c_{p2}	6.88	6.84	1
$\dot{m}$	0.000556	0.000556	1
F	0.48	0.411	1
P_3	0.1	0.1	10
D_e	1.32	1.32	1
T_e	1090	1090	10
T_c, $T_{H_2 f}$	4075	3175	10
θ	20	20	1

Estimates of variable measurement uncertainty were made accounting for the ideal nature and simplifying assumptions of the nonthrust-based data reduction relationships. The estimates were also made based on knowledge of instrumentation measurement limits. These estimates are shown in Table 1 and justifications for these estimates are discussed next.

Uncertainty Estimates for Variables

Variables: R, L, L_t, and D_e. Based upon the dimensions of the absorber unit analyzed, it was decided to make an order of magnitude estimate of the uncertainty of these variables as 1%.

Variable: F. The variable represents thrust in the data reduction relationship. The uncertainty of the thrust has been estimated as 1%; however, the uncertainty in thrust measurement in a solar thermal test facility can range up to approximately 10%.[11]

Variables: k, γ, and c_p. These variables represent thermal conductivity of the fluid, the ratio of specific heats at the chamber conditions, and specific heats associated with the inlet and chamber fluid. Property values are typically obtained from interpolating from a table of data that represents various experimenters' test results. There is a degree of uncertainty associated with the values that must be accounted for.[8] To properly estimate the uncertainty in these property values, the data scatter associated with the original property data should be analyzed. The uncertainty estimates for the property values are set at an order of magnitude of 1% in this study.

Variable: $\dot{m}$. This is the measurement of mass flow rate of the working fluid, H_2. Based on data from different types of

Table 2 UMFs

	Case A						Case B					
	Method, Equation						Method, Equation					
Variable	1, (1)	2, (2)	3, (5)	4, (7)	5, (8)	6, (9)	1, (1)	2, (2)	3, (5)	4, (7)	5, (8)	6, (9)
R	——	——	0.09	——	——	0.12	——	——	0.09	——	——	0.12
L	——	——	0.09	——	——	0.12	——	——	0.09	——	——	0.12
e_1, ε_1	——	——	0.10	——	——	0.13	——	——	0.09	——	——	0.13
e_2, ε_2	——	——	0.01	——	——	0.01	——	——	0.01	——	——	0.01
C	——	——	0.11	——	——	0.15	——	——	0.10	——	——	0.14
L_t	——	——	0.03	——	——	0.04	——	——	0.03	——	——	0.04
k	——	——	0.03	——	——	0.04	——	——	0.03	——	——	0.04
$T_{H_2 i}$	——	——	0.01	——	——	0.01	——	——	0.01	——	——	0.01
a, α	——	——	0.01	——	——	0.01	——	——	0.01	——	——	0.01
P_e	——	0.39	0.40	0.41	0.44	0.45	——	0.45	0.45	0.46	0.49	0.50
P_c	——	0.05	0.05	0.05	——	——	——	0.05	0.05	0.05	——	——
c_v	——	0.58	0.58	0.57	——	——	——	0.56	0.55	0.55	——	——
c_{P1}	——	0.58	0.60	0.57	0.22	0.20	——	0.55	0.58	0.55	0.22	0.20
c_{P2}	——	——	——	——	0.21	0.19	——	——	——	——	0.20	0.19
$\dot{m}$	1.00	0.15	0.18	0.15	0.15	0.19	1.00	0.15	0.19	0.19	0.16	0.20
F	1.00	——	——	——	——	——	1.00	——	——	——	——	——
P_3	——	0.29	0.30	0.30	0.29	0.30	——	0.33	0.33	0.34	0.33	0.33
D_e	——	0.29	0.30	0.30	0.29	0.30	——	0.33	0.33	0.34	0.33	0.33
T_e	——	——	——	——	0.16	0.16	——	——	——	——	0.15	0.16
T_c, $T_{H_2 f}$	——	0.43	——	0.43	0.58	——	——	0.42	——	0.42	0.57	——
θ	——	——	——	0.05	——	——	——	——	——	0.05	——	——

mass flow meters available, an uncertainty for this variable was set at 1%.

Variable: C, CR. This variable represents the concentration ratio at the absorber cavity inlet plane. A variety of methods exist to evaluate a concentration ratio into a cavity.[12] One method involves a geometric ratio that is an average measurement over a certain surface area. Another method involves the use of a peak intensity concentration ratio, (peak intensity/incident solar intensity). For cavity-type absorbers, a measurement of the flux distribution at the focal plane can be used to measure actual heat flux at the absorber cavity opening. Based upon variations among the various approaches to determine CR, a 15% uncertainty on the concentration ratio was used in this analysis.

Variables: $T_{H_2 i}$, T_c, and T_e. These variables represent the average temperatures at the fuel inlet and chamber and nozzle exit locations. Assuming that only one point measurement is employed in each of these readings, the temperature measurements represent the condition at one spatial point. Considering the extreme difficulty of making a chamber temperature measurement, the uncertainty estimates for the average temperatures were set at an order of magnitude of 10%.

Variables: P_e, P_c, and P_3. These variables represent average nozzle exit pressure, pressure of the hydrogen in the chamber, and ambient pressure in the altitude test chamber, respectively. In an actual test situation, the pressures may range from 0.1 to 15 psia. If pressures are measured, they are likely to be static pressures at a wall location, not the average pressure at a cross section. Considering the extremely hostile environment for attempting these measurements, the uncertainty estimates for pressures were set at an order of magnitude of 10%.

Variables: α and ε. These variables represent the emissivities and absorptivities of the various surfaces of the cavity absorber. The radiative properties are functions of temperature and material. In the analysis for methods 3 and 6, it was assumed that the interior surface of the entire cavity exhibited the same emissive and absorptive properties. This was because of the assumptions that the entire cavity was at the same temperature and the heat flux was uniform over the entire inner surface. The way the particular material emits/absorbs radiation is dependent upon the cavity surface temperature. For materials proposed for solar thermal propulsion, the absorptivity and emissivity along the internal surfaces of the cavity absorber can vary as much as 50% over a temperature range of 2300–5000°R (Ref. 13). An uncertainty of 50% was estimated for these variables.

Results

The UMF results for all six methods are shown in Table 2 for cases A and B. As expected, for method 1 (in which thrust and mass flow rate are measured directly) the UMFs are 1.0; this means that the uncertainties in thrust and mass flow rate are neither magnified nor diminished as they propagate into the uncertainty in specific impulse. For methods 2–6, all UMFs are less than 1.0. This fortuitous result means that the uncertainties in all of the variables that must be measured or otherwise determined are diminished as they propagate into the uncertainty in specific impulse. The Isps were evaluated and they ranged between 820–840 s for case A, and between 740–750 s for case B when considering nonthrust-based methods.

The UMFs in methods 2–6 have a large range in magnitude (from 0.58 down to 0.005), illustrating the usefulness of such an analysis. Having such information in the initial planning phase of an experiment allows the determination of variables that have the greatest potential to adversely affect the uncertainty in the experimental result, thus allowing resources to be focused on the measurement of those variables at the beginning of the experimental program.

Table 3 shows the UPC results, which can be obtained once uncertainties have been estimated for all of the variables in the data reduction equations. For method 1, the 1% uncertainties estimated for thrust and mass flow rate measurements contribute equally to the 1.4% uncertainty in the specific impulse. (For a 10% uncertainty in the thrust measurement, the uncertainty in the specific impulse would be 10%.)

Methods 2, 4, and 5 are those that assume a measurement of fluid temperature in the chamber can be made, and the UPCs indicate that the uncertainty contributions of the chamber temperature and nozzle exit plane pressure measurements are the dominant ones (which one is greater varies with the method used and from case A to case B). The resulting uncertainties in specific impulse range from about 6.6 to 8.4%. The uncertainties in specific impulse would still range from 5% to over 6% if the 10% uncertainty estimate in chamber temperature measurement was set to 0% and all of the other uncertainties remained the same. This means that the pressure at the nozzle

Table 3 UPCs

	Case A						Case B					
	Method, Equation						Method, Equation					
Variable	1, (1)	2, (2)	3, (5)	4, (7)	5, (8)	6, (9)	1, (1)	2, (2)	3, (5)	4, (7)	5, (8)	6, (9)
R	——	——	0.02	——	——	0.02	——	——	0.01	——	——	0.02
L	——	——	0.02	——	——	0.02	——	——	0.01	——	——	0.02
e_1, ε_1	——	——	44.06	——	——	53.62	——	——	38.65	——	——	48.91
e_2, ε_2	——	——	0.00	——	——	0.00	——	——	0.00	——	——	0.00
C	——	——	4.88	——	——	5.94	——	——	4.16	——	——	5.26
L_t	——	——	0.00	——	——	0.00	——	——	0.00	——	——	0.00
k	——	——	0.00	——	——	0.00	——	——	0.00	——	——	0.00
$T_{H_2 i}$	——	——	0.01	——	——	0.01	——	——	0.01	——	——	0.01
a, α	——	——	0.52	——	——	0.64	——	——	0.34	——	——	0.43
P_e	——	35.70	31.15	36.79	30.02	25.12	——	40.56	35.73	41.65	34.60	29.13
P_c	——	0.51	0.43	0.49	——	——	——	0.42	0.36	0.40	——	——
c_v	——	0.77	0.65	0.74	——	——	——	0.63	0.54	0.60	——	——
c_{P1}	——	0.77	0.72	0.74	0.08	0.05	——	0.63	0.59	0.60	0.07	0.05
c_{P2}	——	——	——	——	0.07	0.04	——	——	——	——	0.06	0.04
$\dot{m}$	50.00	0.05	0.06	0.05	0.03	0.05	50.00	0.06	0.07	0.06	0.04	0.05
F	50.00	——	——	——	——	——	50.00	——	——	——	——	——
P_3	——	19.90	17.29	20.35	13.34	11.16	——	21.86	19.20	22.30	15.38	12.95
D_e	——	0.20	0.17	0.20	0.13	0.11	——	0.22	0.19	0.22	0.15	0.13
T_e	——	——	——	——	3.77	3.28	——	——	——	——	3.35	2.91
T_c, $T_{H_2 f}$	——	42.17	——	40.58	52.58	——	——	35.62	——	34.18	46.47	——
θ	——	——	——	0.00	——	——	——	——	——	0.01	——	——
UI_{sp}, %	1.41	6.57	7.14	6.67	8.04	8.93	1.41	7.00	7.55	7.11	8.38	9.24

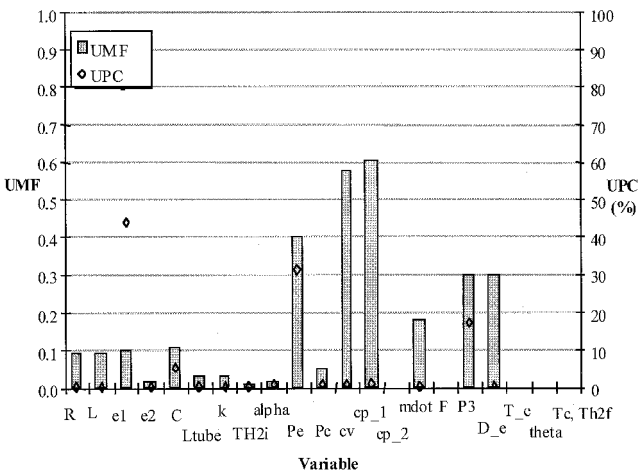

Fig. 4 UMF/UPC values vs variable for method 3 (case A).

exit plane (0.15 psia in this study) must be determined better than ±10% (±0.015 psi in this study) for significant improvement in the specific impulse uncertainty, even if a reliable measurement of chamber temperature could be made.

Methods 3 and 6 are those that incorporate additional heat transfer analysis assumptions to remove the requirement for a measurement of chamber temperature, and the UPCs indicate that the uncertainty contributions from the estimated emissivity of the interior wall of the cavity and the nozzle exit plane pressure measurements are the dominant ones. The resulting uncertainties in specific impulse range from about 7 to 9.2%. The statements made about the exit plane pressure measurement in the preceding paragraph also apply here. In addition, consideration of the impact of the assumption that the interior wall of the cavity is isothermal (along with all the other factors that make estimating an emissivity so difficult) makes the 50% uncertainty estimate for emissivity defensible as a ball-park figure in the authors' opinion. It thus seems unlikely that methods 3 and 6 could yield a specific impulse value with an uncertainty of less than 7% or so.

Both the UMF and UPC values for method 3, case A are plotted in Fig. 4 to illustrate the information available from an uncertainty analysis at different stages of an experimental program. The UMFs indicate the specific heat values and the exit pressure values as the largest potential contributors to specific impulse uncertainty in the initial portion of the planning phase before uncertainty estimates have been made. Once estimates (perhaps only order-of-magnitude estimates) of uncertainties are available, the UPCs indicate the largest contributors to the uncertainty in the result. In this instance, the cavity surface emissivity appears as the largest contributor and the contributions of the specific heat uncertainties are negligible, the opposite of the potential effects shown by the UMFs.

In conclusion, for the particular operating conditions and engine design specified in this study, it appears unlikely that a specific impulse determination can be made with an uncertainty less than 5–6% when using methods 2–6. Method 1, utilizing thrust and flow rate measurements, has the potential for a 2% or so uncertainty in specific impulse determination if the difficult problems[11] affecting the thrust measurement can be solved.

Acknowledgments

This research was performed under McDonnell Douglas Aerospace/Solar Thermal Upper Stage Technology Demonstration Program Contract A3-Y903-JMH-95-003. The authors would also like to recognize U.S. Air Force Phillips Laboratory, Edwards Air Force Base, California, and NASA/MSFC technical advisors for their assistance.

References

[1]Stewart, J. F., and Martin, J. A., "Dual Fuel Solar Thermal Propulsion for LEO to GEO Transfer: Ideal Rocket Analysis," AIAA 95-2840, July 1995.

[2]Sutton, G. P., *Rocket Propulsion Elements*, 6th ed., Wiley, New York, 1992.

[3]Laug, K., "The Solar Propulsion Concept is Alive and Well at the Astronautics Laboratory," Chemical Propulsion Information Agency, Publ. 515, Vol. 1, 1989.

[4]Hastings, L., and Gerrish, H., STUSTD Program Quarterly Review Presentation, NASA/MSFC, 1995.

[5]Markopoulos, P. "An Uncertainty Assessment of Performance Evaluation Methods for Solar Thermal Absorber/Thruster Testing," M.S. Thesis, Univ. of Alabama, Huntsville, AL, 1996.

[6]Shoji, J. M., "Solar Rocket Component Study," Air Force Rocket Propulsion Lab., TR-84-057, 1984.

[7]Pearson, J. B., Landrum, D. B., and Hawk, C. W., "Parametric

Study of Solar Thermal Rocket Nozzle Performance,'' *Proceedings of the 1995 ASME/JSME/JSES International Solar Energy Conference*, 1995.

[8]Coleman, H. W., and Steele, W. G., *Experimentation and Uncertainty Analysis for Engineers*, Wiley, New York, 1989.

[9]Blevins, J. A., and Coleman, H. W., ''An Assessment of Connected-Pipe Ramjet Testing,'' AIAA Paper 95-3074, July 1995.

[10]Hudson, S. T., and Coleman, H. W., ''A Preliminary Assessment of Methods for Determining Turbine Efficiency,'' AIAA Paper 96-0101, Jan. 1996.

[11]Holmes, M., and Laug, K., STUSTD Program Quarterly Review, USAF Edwards AFB, May 1995.

[12]Kreider, J. F., *Medium and High Temperature Solar Processes*, Academic, New York, 1979.

[13]*Handbook of Chemistry and Physics*, 64th ed., CRC Press, Boca Raton, FL, 1984.